Role of N-Type Voltage-Dependent Calcium Channels in Autoimmune Optic Neuritis

Ivana Gadjanski, PhD, [1,2] Susann Boretius, PhD,[3] Sarah K. Williams, PhD,[4] Paul Lingor, MD,[1,5]
Johanna Knöferle, MD,[1] Muriel B. Sättler, MD,[1] Richard Fairless, PhD,[4] Sonja Hochmeister, MD, PhD,[6]
Kurt-Wolfram Sühs, MD,[4] Thomas Michaelis, PhD,[3] Jens Frahm, PhD,[3] Maria K. Storch, MD,[6]
Mathias Bähr, MD,[1,5] and Ricarda Diem, MD[4]

Objective: The aim of this study was to investigate the role of voltage-dependent calcium channels (VDCCs) in axon degeneration during autoimmune optic neuritis.
Methods: Calcium ion (Ca^{2+}) influx into the optic nerve (ON) through VDCCs was investigated in a rat model of optic neuritis using manganese-enhanced magnetic resonance imaging and in vivo calcium imaging. After having identified the most relevant channel subtype (N-type VDCCs), we correlated immunohistochemistry of channel expression with ON histopathology. In the confirmatory part of this work, we performed a treatment study using ω-conotoxin GVIA, an N-type specific blocker.
Results: We observed that pathological Ca^{2+} influx into ONs during optic neuritis is mediated via N-type VDCCs. By analyzing the expression of VDCCs in the inflamed ONs, we detected an upregulation of α_{1B}, the pore-forming subunit of N-type VDCCs, in demyelinated axons. However, high expression levels were also found on macrophages/activated microglia, and lower levels were detected on astrocytes. The relevance of N-type VDCCs for inflammation-induced axonal degeneration and the severity of optic neuritis was corroborated by treatment with ω-conotoxin GVIA. This blocker led to decreased axon and myelin degeneration in the ONs together with a reduced number of macrophages/activated microglia. These protective effects were confirmed by analyzing the spinal cords of the same animals.
Interpretation: We conclude that N-type VDCCs play an important role in inflammation-induced axon degeneration via two mechanisms: First, they directly mediate toxic Ca^{2+} influx into the axons; and second, they contribute to macrophage/microglia function, thereby promoting secondary axonal damage.

Ann Neurol 2009;66:81–93

Multiple sclerosis (MS) is an inflammatory, demyelinating disease of the central nervous system, accompanied by neurodegeneration that determines chronic disability.[1,2] Studies in humans and animal models[3–8] have shown that axonal and neuronal damage starts during early disease stages. One of the most common clinical manifestations of MS is optic neuritis.[9]

Experimental autoimmune encephalomyelitis (EAE) is the principal model of MS.[10] We have previously demonstrated that myelin oligodendrocyte glycoprotein–induced EAE in brown Norway rats leads to optic neuritis in 80 to 90% of animals with consecutive axonal degeneration of the optic nerve (ON) and apoptosis of retinal ganglion cells (RGCs).[6–8,11]

The mechanisms of axonal degeneration in autoimmune inflammation are not fully understood but are likely to involve an accumulation of calcium ions (Ca^{2+}) in the axons. Indeed, several studies emphasize the involvement of Ca^{2+} in axonal degeneration in trauma,[12] anoxia,[13–15] ischemia,[16] and inflammatory models.[4] Under these pathological conditions, Ca^{2+} enters axons or neurons via ion-specific transport mechanisms such as voltage-dependent calcium channels (VDCCs), glutamate receptors, and/or reverse operation of the Na^+/Ca^{2+} exchanger. In addition to a possible direct relevance for axonal degeneration in autoimmune inflammation, Ca^{2+} entry and VDCC activity may also be important for immune cell function: It has been shown that macrophages/microglia change membrane properties on activation.[17,18] Further, it is

known that T lymphocytes express beta regulatory subunits of VDCCs.[19]

In our study, we focused on the role of VDCCs during myelin oligodendrocyte glycoprotein–induced optic neuritis. We used manganese (Mn^{2+})-enhanced magnetic resonance imaging (MRI) in combination with VDCC blockers to identify those channels responsible for pathological Ca^{2+} influx into the ON. In parallel, we have performed in vivo Ca^{2+} imaging of the ON, as well as expression analyses of VDCCs. The significance of an increased Ca^{2+} influx via N-type VDCCs for neurodegeneration, demyelination, and inflammation was further confirmed by administration of ω-conotoxin GVIA (ω-CTX), a specific antagonist of N-type VDCCs.

Materials and Methods

Rats
A total of 65 female brown Norway rats (8–10 weeks; Charles River, Sulzfeld, Germany) were used. Animal experiments have been approved by the authorities of Braunschweig, Germany.

Experimental Autoimmune Encephalomyelitis Model
Recombinant rat myelin oligodendrocyte glycoprotein was synthesized and injected as described elsewhere.[20] Rats were scored daily for clinical signs of EAE.[6] The cumulative score was calculated as the sum of daily scores.

Quantification of Retinal Ganglion Cell Density
A week before immunization, RGCs were labeled by injection of fluorogold into both superior colliculi.[7] After the in vivo part of the experiments, rats were killed with CO_2 and perfused with 4% paraformaldehyde in phosphate-buffered saline. Retinas were flat-mounted onto glass slides and RGC densities determined as described previously.[6]

Optic Nerve Histopathology
Animals were perfused with 4% paraformaldehyde, and ONs were embedded in paraffin. Histological evaluation was performed on 0.5μm sections stained with Luxol fast blue (LFB) and Bielschowsky silver impregnation. Demyelinated areas were determined as a percentage of the ON cross section. The surface area of the ON was measured using the AxioVision-4.5 software (Zeiss, Göttingen, Germany). Overview (200-fold) and high-magnification photographs (1,000-fold) were made with a charge-coupled device camera (Color View-II) using an Axioplan-2 microscope (Zeiss). Axonal densities were determined in ON cross sections stained with Bielschowsky silver impregnation by point sampling using a 25-point Olympus grid. Point sampling overcomes density artefacts arising with increased ON areas.[2] Seventy-five points were superimposed on the whole of the ON cross section. The number of points crossing axons was measured as the fraction of the number of points of the stereological grid.[2] Axon reduction is given as the percentage of axon density compared with the average axon density in healthy ONs.

Neuropathological examinations were performed in a blinded manner.

To differentiate between axonal fibers with larger diameters ($>2μm^2$) and those with smaller diameters ($\leq2μm^2$), we performed a slightly modified technique for fiber counts as DeLuca and colleagues[21] described previously. In brief, high-magnification photographs ($\times1000$) were digitized and enhanced (AxioVision-4.5; Zeiss). We then performed manual counts of axons to exclude axonal spheroids from quantification. This was done to avoid a bias toward fibers of larger diameter, which would not have been possible using an Image software program for fiber counts. Manual counts of axons were performed in a blinded manner by two independent investigators with long-standing experience in the field of neuropathology.

Immunohistochemistry on Optic Nerves
Immunohistochemistry was performed on serial sections of paraffin-embedded ONs. As primary antibodies we used rabbit anti-α_{1B} (1:1,000; Sigma-Aldrich, Taufkirchen, Germany), mouse anti–β-amyloid precursor protein (β-APP, Chemicon, Temecula, CA; 1:1,000), mouse anti-CD68 (1:500, ED1; Serotec, Oxford, United Kingdom), mouse anti–endothelial monocyte-activating polypeptide II (1:100; EMAP II; Abcam, Cambridge, United Kingdom), mouse anti–glial fibrillary acidic protein (1:100; GFAP; Dianova, Hamburg, Germany), mouse anti-myelin-2′,3′-cyclic-nucleotide-3′-phosphodiesterase (myelin-CNPase) (1:200, SMI-91; Covance Princeton, NJ), mouse anti-phosphorylated neurofilament (1:1,000, SMI-31; Covance), or mouse anti-nonphosphorylated neurofilament (1:1,000, SMI-32; Covance). Secondary biotinylated antibodies (Vector, Burlingame, CA) were used as follows: goat anti–rabbit IgG (1:200), goat or horse anti–mouse IgG (1:200). In addition, we used Cy3-labeled goat anti–rabbit IgG (1:600; Jackson Immunoresearch, West Grove, PA), and Alexa 488–labeled goat anti–mouse IgG (1:400; Molecular Probes, Leiden, the Netherlands). Control sections were incubated without primary antibodies. Spinal cord sections served as positive controls.[4] Stereological quantitative analyses of ED1- and α_{1B}-labeled serial sections were performed by counting labeled cells in 9 microscopic fields of 62,500μm², each defined by a morphometric grid. The counts were performed by two investigators following a blind protocol.

Analysis of Spinal Cord Lesions
Histological evaluation was performed on paraformaldehyde-fixed, paraffin-embedded sections of spinal cords. Paraffin sections were stained with hematoxylin and eosin, LFB, and Bielschowsky silver impregnation to assess inflammation, demyelination, and axonal pathology. In adjacent serial sections, immunohistochemistry was performed with an antibody against β-APP (1:1,000; Chemicon) and macrophages/activated microglia (ED1; 1:1,000). Bound primary antibody was detected with a biotin-avidin technique as described previously.[22] Control sections were incubated in the absence of primary antibody or with nonimmune rabbit serum. The following histopathological parameters were analyzed. The degree of demyelination was evaluated semiquantitatively for

the spinal cord sections and scored as follows: traces of perivascular or subpial demyelination (0.5), marked perivascular or subpial demyelination (1), confluent perivascular or subpial demyelination (2), demyelination of half spinal cord cross section (3), and transverse myelitis (4). Quantitative assessment of ED1-positive cells and β-APP–positive axons was determined as described previously.[23,24] In brief, β-APP–positive axons were evaluated by overlaying a morphometric grid on ED1/β-APP–stained spinal cord cross sections at a magnification of ×900. Values are expressed as positive cells or axons per square millimeters per total spinal cord cross section (axons/mm^2/total spinal cord cross section). Two investigators performed the neuropathological examinations independently and in a blinded manner.
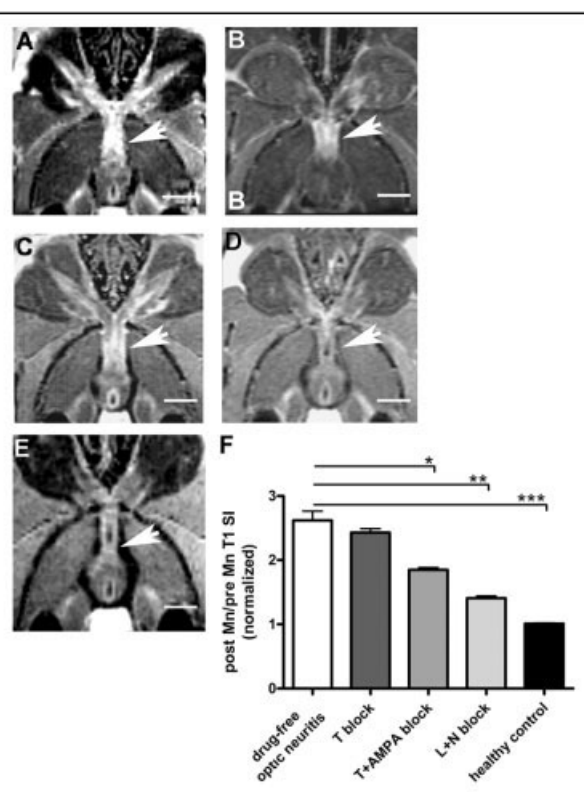
Magnetic Resonance Imaging

Thirty-three animals underwent MRI at day 14 after immunization. Anesthesia was induced by medetomidine (0.25mg/kg subcutaneously; Pfizer, Berlin, Germany) and ketamine (25mg/kg intravenously; Medistar, Hanover, Germany). After relaxation, the animals were intubated as described previously.[25]

MRI measurements were performed at 2.35 Tesla using an MRBR 4.7/400mm magnet (Magnex Scientific, Abington, United Kingdom) equipped with a DBX system (Bruker Biospin, Ettlingen, Germany).[25] After acquisition of precontrast T1-weighted images, MnCl$_2$ (50μmol/kg; Sigma-Aldrich) was applied in an aqueous solution via a vein catheter. Mn^{2+}-enhanced, T1-weighted MRI was performed 10 minutes, 24 hours, and 48 hours after MnCl$_2$ administration. Some animals additionally received the following VDCC or α-amino-3-hydroxyl-5-methyl-4-isoxazole-propionate (AMPA)/kainate receptor blockers (single-bolus injection over 30–60 seconds) immediately before application of MnCl$_2$: diltiazem (20mg/kg intraperitoneally; Sigma-Aldrich), ω-CTX (10μg/kg intravenously; Anaspec, San Jose, CA), amlodipine (5mg/kg orally; LKT-Laboratories, St. Paul, MN), amiloride (100μmol/kg intravenously; Sigma-Aldrich), ω-agatoxin IVA (20μg/kg intravenously; Alomone, Jerusalem, Israel), or NBQX (30mg/kg intraperitoneally; Tocris-Bioscience, Ellisville, MO). Drug concentrations were chosen as described previously.[26–30]

For quantitative image analyses, MRI sections parallel to the ON (see Supplemental Fig 1A) were used to determine a suitable region of interest. Region-of-interest analyses were based on MRI signal intensities (SI) in the ON normalized to the intensity of nearby gray matter using Paravision 3.2 (Bruker Biospin, Ettlingen, Germany) (see Supplemental Fig 1B). The ratio of the normalized SI after and before application of MnCl$_2$ was calculated to determine the efficiency of the applied antagonists to block respective Ca^{2+} channels.

In Vivo Calcium Imaging

Animals were anesthetized by chloralhydrate (420mg/kg intraperitoneally). Using a Hamilton syringe, we injected 3μl Oregon-Green-488 BAPTA-1 AM ester (OGB) into the vitreous body. OGB is taken up by RGCs, the cell bodies of the ON axons. After entering the cytoplasm of RGCs, OGB is hydrolyzed to a form that cannot easily pass through the cell membrane. Therefore, most of the OGB transported an-

Fig 1. T1-weighted magnetic resonance images obtained 10 minutes after MnCl$_2$ application show the effects of type-specific, voltage-dependent calcium channel (VDCC) blockers and an α-amino-3-hydroxyl-5-methyl-4-isoxazole-propionate (AMPA) receptor antagonist on Mn^{2+}-induced enhancement (MIE) within the optic nerves (ONs). (A) Drug-free optic neuritis. (B) T-type VDCC blockade did not reduce MIE. (C) The combination of a T-type VDCC blocker and an AMPA receptor antagonist led to reduction of MIE (p < 0.05). (D) Inhibition of L- and N-type VDCCs led to a highly significant reduction of MIE (p < 0.01). (E) MIE was not observed in the ONs of a healthy sham-immunized rat. (F) Normalized signal intensity (SI) obtained from T1-weighted images (post Mn/pre Mn T1 SI) of the inflamed ONs without blocker (drug-free optic neuritis), with amiloride (T block), with amiloride and NBQX (T+AMPA block), with amlodipine (L+N block), and of the ONs of healthy sham-immunized rats (healthy control). Arrowheads point to the left optic nerve in each animal. Error bars represent standard error of the means. *p < 0.05; **p < 0.01; ***p < 0.001. Scale bars = 2mm.

terogradely along ON axons is maintained within the intracellular space of the ON axons. After 2 hours, the orbita was opened and the ON exposed by longitudinal incision of the nerve sheath. A tie of fine surgical thread (10/0, Ethilon, Johnson Medical GmbH, Norderstedt, Germany) was placed around the ON to make sure that the tissue visualized was indeed the ON.

The rat was placed below an objective (40x/0.8WPh2; Zeiss), and the space between the objective and the ON was filled with 0.9% NaCl. OGB was excited at 488nm and collected through a 522nm band-pass filter using a fluorescence

microscope (Axioplan-2; Zeiss). Fifty images (1/sec) were taken before inducing depolarization by intravitreal injection of 10μl of a KCl solution (160mM) to quantify the extent of photobleaching. Thirty minutes before inducing depolarization, ω-CTX (Mobitec, Göttingen, Germany) was applied topically to the ON in a dose of 3μg per ON.[31]

The data were analyzed with ImageJ 1.36b (http://rsb.info.nih.gov/ij/) measuring the integrated density (gray values of pixels) in a representative region of interest of the ON. As the baseline fluorescence activity varied from nerve to nerve, the baseline fluorescence intensity of each nerve was set to 100%. The maximum fluorescence peak was set in relation to this baseline. The ON has some minor autofluorescence, which is much lower than the baseline fluorescence of the nerve loaded with OGB. Similarly, the baseline fluorescence of the nerve loaded with OGB was set in relation to the maximum fluorescence peak in each experiment and, therefore, should not have an effect on the calcium-triggered increase of fluorescence activity after KCl injection.

Intracerebroventricular Infusion
Sixteen rats were implanted with miniosmotic pumps and the respective brain infusion kits (model 2004; Alzet, Cupertino, CA). ω-CTX (6μM) was diluted in artificial cerebrospinal fluid (Harvard Apparatus, Dover, MA). The control group received pumps containing only artificial cerebrospinal fluid. The pumps were primed for 40 hours at 37°C in 0.9% saline and implanted subcutaneously in the midscapular region. The tip of the infusion kit was placed into the right lateral ventricle (0.9mm caudal and 1.4mm lateral to bregma, 3.6mm below the dura mater). The minipumps yielded a constant rate of 0.25μl/hr for 23 days in the pretreatment groups and for 8 days in the late-treatment groups. During these experiments, ω-CTX was delivered at a concentration of 1.5pmol/hr according to published protocols.[32] After explantation of the pumps, the residual volume was measured.

Statistics
Mn^{2+}-induced enhancement (MIE) in the pilot MRI study was compared by one-way analysis of variance followed by Tukey's multiple-comparison Test. For larger samples, as in the main MRI study, we used Kruskal–Wallis nonparametric analysis of variance followed by Dunn's post hoc procedure. Histopathological and calcium imaging data, RGC densities, and neurological scores were analyzed by the nonparametric Mann–Whitney two-tailed test. The Spearman's two-tailed test was used to correlate α_{1B} expression with demyelination or axonal reduction. All statistical analyses were performed using GraphPad Prism software, version 4.00 (GraphPad Software, San Diego, CA).

Results

High-Voltage–Activated Calcium Channels Mediate Mn^{2+} Uptake into the Optic Nerve
Mn^{2+} is an analog of Ca^{2+} and serves as an MRI contrast agent. We injected $MnCl_2$ to detect pathophysiological changes related to Ca^{2+} influx in rats with optic neuritis by MRI. To investigate possible routes of

$MnCl_2$ entry into the ON, we modified a previously established MRI protocol.[25] VDCC and AMPA/kainate receptor antagonists were applied immediately before administration of $MnCl_2$.

Initially, the effects of the following antagonists were investigated: (1) an AMPA/kainate receptor antagonist (NBQX), (2) a high-voltage–activated VDCC antagonist specific for L- and N-type VDCCs (amlodipine), and (3) a low-voltage–activated VDCC antagonist acting on T-type VDCCs (amiloride).

Application of the T-type blocker still allowed for an enhancement of Mn^{2+} within the inflamed ON in magnetic resonance images taken 10 minutes after application of $MnCl_2$ (Figs 1B, F). However, significantly reduced MIE was seen after application of the T-type blocker in combination with the AMPA/kainate receptor antagonist ($p < 0.05$; see Figs 1C, F). A highly significant reduction of MIE could be observed after application of the L+N blocker ($p < 0.01$; see Figs 1D, F) when compared with rats with optic neuritis that received $MnCl_2$ alone (see Figs 1A, F). Healthy ONs of sham-immunized rats (n = 6) showed no MIE after Mn^{2+} application, which was significantly different in comparison with untreated inflamed ONs ($p < 0.001$) (see Figs 1E, F).
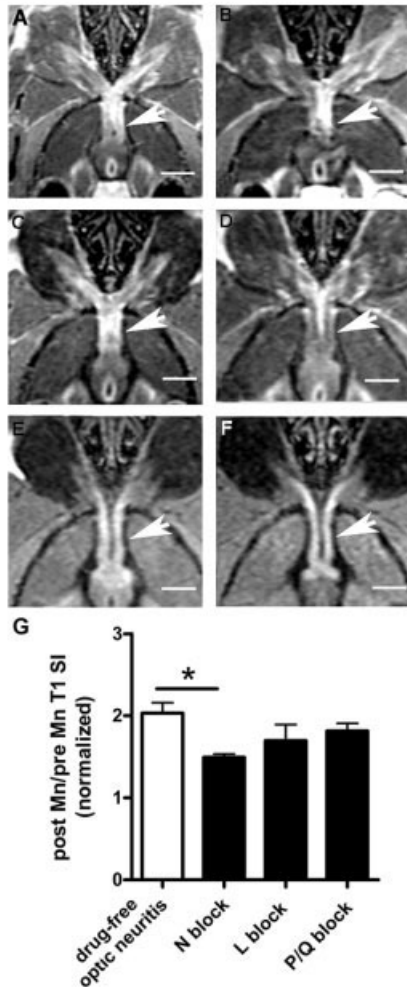
The normalized SI of the ONs was measured before and 10 minutes after application of $MnCl_2$, and their ratio was used to quantify the effect of the antagonists. Mean values ± standard error of the mean (see Fig 1F) were 2.62 ± 0.14 in rats with drug-free optic neuritis (n = 4), 2.43 ± 0.06 in animals receiving the T-type blocker (n = 3), 1.85 ± 0.04 after combined application of the T-type blocker and the AMPA/kainate receptor antagonist (n = 3), 1.40 ± 0.04 for the L+N blocker (n = 3), and 1.01 ± 0.01 in healthy sham-immunized animals (n = 6).

Mn^{2+} Enters the Optic Nerve via N-Type Voltage-Dependent Calcium Channels
Because the most prominent inhibition of Mn^{2+} uptake was observed after application of the L+N-type blocker, our objective was to further dissect the high-voltage–activated VDCCs involved in Mn^{2+} influx, namely, L-type, P/Q-type, and N-type, with the use of specific antagonists. These included diltiazem, an inhibitor of L-type VDCCs,[29] ω-CTX, a blocker for N-type VDCCs,[28] and ω-agatoxin IVA, an inhibitor of P/Q-type VDCCs.[28] The antagonists were applied to those animals with abnormalities in T1-weighted magnetic resonance images (increased ON diameter and hypointense T1-weighted SI).

A T1-weighted image of inflamed ONs of an untreated animal 10 minutes after Mn^{2+} application is presented in Figure 2A. Figures 2B to D show ONs of rats that additionally received the L-type (see Fig 2B), the P/Q-type (see Fig 2C), or the N-type

blocker (see Fig 2D). Whereas the normalized SI ratios in animals receiving the L-type (1.70 ± 0.20; $n = 8$) or P/Q-type blocker (1.82 ± 0.09; $n = 9$), although reduced, did not significantly differ from drug-free optic neuritis (2.03 ± 0.13; $n = 14$), MIE in the ONs was significantly reduced after application of the N-type blocker (1.49 ± 0.04; $n = 7$; $p < 0.05$; see Fig 2G). Magnetic resonance images presented in Figures 2A to D were taken 10 minutes after administration of $MnCl_2$.

In this context, it should be mentioned that the half-life of ω-CTX is 4.61 ± 0.59 hours.[33] Therefore, MRI performed 24 and 48 hours later demonstrated an MIE also in ONs with suppressed enhancement 10 minutes after injection of the N-type blocker. Quantitative analyses showed that the normalized SI relative to the precontrast image of the ONs both at 24 (1.35 ± 0.04; $n = 5$) and 48 hours after $MnCl_2$ application (1.14 ± 0.09; $n = 5$) (see Figs 2E, F) was not significantly different from that of animals that received $MnCl_2$ without a blocker (1.42 ± 0.11 at 24 hours; $n = 5$; 1.41 ± 0.12 at 48 hours; $n = 3$).

N-Type Voltage-Dependent Calcium Channel Expression Correlates with Demyelination

Because blockade of N-type VDCCs reduced Mn^{2+} uptake into inflamed ONs, N-type VDCC expression was investigated further. Immunohistochemistry for α_{1B}, the pore-forming subunit of N-type VDCCs, showed a significant difference in both degree and pattern of N-type VDCC expression between healthy and inflamed ONs. In healthy, myelinated ONs (Fig 3A), a modest degree of α_{1B} immunoreactivity was detected (see Fig 3B) and quantified as the number of α_{1B}-positive sites per square millimeter (493.22 ± 14.79; $n = 8$) (see Fig 3F). However, a significant upregulation of expression was seen during optic neuritis ($1,323.38 \pm 79.51$; $n = 10$; see Figs 3C, D) compared with the ONs of sham-immunized rats ($p < 0.001$) (see Fig 3F). Furthermore, a significant correlation between the number of α_{1B}-positive sites per square millimeter and the percentage of demyelination was detected ($r = 0.76$; $p < 0.001$; $n = 26$) (see Fig 3G). A significant correlation was further observed between the number of α_{1B}-positive sites per square millimeter and the percentage of axonal reduction ($r = 0.66$; $p < 0.001$; $n = 26$) (see Fig 3H). In parallel with the α_{1B} staining of serial ON sections, spinal cord sections from healthy rats served as positive controls (see Fig 3E).[4]

N-Type Voltage-Dependent Calcium Channel Expression Correlates with Immunoreactivity for β-Amyloid Precursor Protein, Nonphosphorylated Neurofilament, and with ED1- and EMAP II–Positive Macrophages/Microglia

We further investigated the relation between the expression of α_{1B} and β-APP, a marker of disturbed axonal transport, in optic neuritis. Fluorescence microscopy showed a colocalization of α_{1B} and β-APP, as shown in Figure 4A. In addition, we detected expression of α_{1B} in nonphosphorylated ON axons stained

Fig 2. T1-weighted magnetic resonance images obtained after $MnCl_2$ application demonstrating the effects of type-specific, high-voltage–activated (HVA) voltage-dependent calcium channel (VDCC) blockers on Mn^{2+}-induced enhancement (MIE) within the inflamed optic nerves (ONs). (A–D) Images were taken 10 minutes after application of $MnCl_2$ without a blocker (A), with the L-type VDCC blocker (B), with the P/Q-type VDCC blocker (C), and with the N-type VDCC blocker (D). Note that application of the N-type VDCC blocker suppresses MIE within the ONs. (E, F) After degradation of the N-type VDCC blocker (after 24 hours), MIE of the inflamed ONs recovers (E) and retains up to 48 hours (F). (G) Normalized signal intensities (SIs) of the ONs without blocker (drug-free optic neuritis), with ω-conotoxin GVIA (ω-CTX) (N block), with diltiazem (L block), and with ω-agatoxin IVA (P/Q block). Arrowheads point to the left optic nerve in each animal. Error bars represent standard error of the means (*p < 0.05). Scale bars = 2mm.
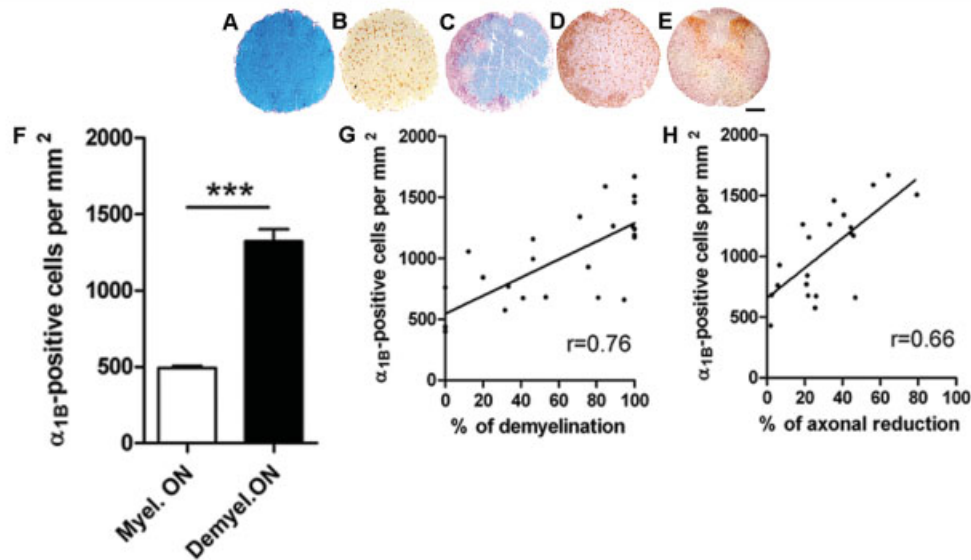
Fig 3. Expression of the pore-forming subunit of N-type voltage-dependent calcium channels (VDCCs) (α_{1B}) in the optic nerves (ONs) of healthy rats and rats with optic neuritis. (A) Luxol fast blue (LFB) staining of a healthy ON, showing complete myelination (blue area). (B) Adjacent serial section of the ON shown in (A) stained for α_{1B}. (C) LFB staining of a representative ON from a rat with myelin oligodendrocyte glycoprotein (MOG)–induced optic neuritis. (D) Adjacent serial section of the ON shown in (C) stained for α_{1B}. Note the upregulation of α_{1B} in the demyelinated areas. (E) Cross section of a healthy rat spinal cord, showing intense α_{1B} immunoreactivity in regions of high synaptic density. Spinal cord served as control for the efficacy of the α_{1B} staining. (F) Quantification of α_{1B}-positive sites per square millimeter in myelinated and demyelinated ONs. ***$p < 0.001$. (G) Correlation between the numbers of α_{1B}-positive sites per square millimeter and the percentage of demyelination. (H) Correlation between the numbers of α_{1B}-positive sites per square millimeter and the percentage of axonal reduction. Scale bar $= 100\mu m$ (A–D); $400\mu m$ (E).

with SMI-32 (see Fig 4C) indicating that N-type VDCCs are not only expressed in areas of transport failure but also in nonspheroided, degenerating axons. In contrast, no expression of α_{1B} was seen in healthy ON axons stained with SMI-31, a marker of phosphorylated, intact axons (see Fig 4B).

However, many α_{1B}-positive cells were β-APP– or SMI-32–negative, suggesting that another cell type also expresses N-type VDCCs. Double immunohistochemistry for α_{1B} and ED1, as well as for α_{1B} and EMAP II, another marker of macrophages/activated microglia,[34,35] showed strong colocalization (see Figs 4E, F), but there were also a few α_{1B}-immunoreactive cells that were ED1- and EMAP II–negative. Furthermore, some immunoreactivity was detected on astrocytes (see Fig 4D). In contrast, no colocalization was seen between α_{1B} and either CNPase, a marker of oligodendrocytes (see Figs 4G, H), or CD3, a marker for T lymphocytes (data not shown).

ω-CTX Suppresses Ca²⁺ Influx into the Inflamed Optic Nerve

To investigate whether ω-CTX not only suppresses Mn^{2+} but also Ca^{2+} influx into the ON, we performed in vivo Ca^{2+} imaging in rats 15 days after immunization. Measurements of fluorescence signal in-

tensity changes after KCl-induced depolarization demonstrated a significantly increased influx of Ca^{2+} into the ONs in rats with optic neuritis (112.3 ± 2.4%; n = 13; Figs 5C, D, G) in comparison with ONs in healthy sham-immunized animals (104.7 ± 0.9%; n = 9; $p < 0.05$; see Figs 5A, B, G). After application of ω-CTX to inflamed ONs, the depolarization-induced influx of Ca^{2+} was significantly inhibited (100.4 ± 0.2%; n = 7; see Figs 5E–G; $p < 0.001$) in comparison with inflamed ONs after application of NaCl. Furthermore, inflamed ONs after application of ω-CTX showed significantly less fluorescence signal intensity than healthy ONs ($p < 0.01$; see Fig 5G).

Application of ω-CTX Ameliorates Optic Neuritis

After observing that N-type VDCCs are upregulated in degenerating axons and are expressed on macrophages/microglia during optic neuritis, we tested whether these phenomena play a role in neurodegeneration. ω-CTX was continuously applied via osmotic minipumps to the cerebrospinal fluid, and the extent of neurodegeneration was subsequently assessed by histopathology. Two treatment paradigms were compared: In the first two groups ("PRE"), delivery of ω-CTX or vehicle started 2 days before immunization and was continued
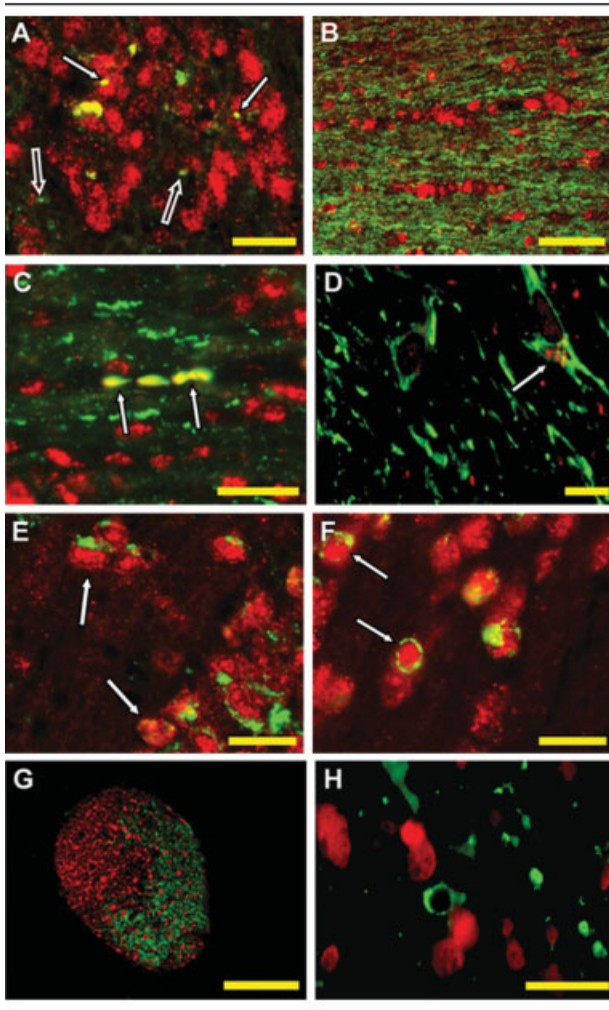
Fig 4. Immunofluorescence of α_{1B} in healthy optic nerves and during optic neuritis. (A) Colocalization of β-amyloid precursor protein (β-APP) (green) and α_{1B} (red) as seen in a merged fluorescence microscopy image (closed arrows indicate colocalization of β-APP and α_{1B}; open arrows indicate α_{1B}-negative, β-APP–positive axonal profiles). (B) Healthy optic nerve (ON) stained with the phosphorylated neurofilament marker SMI-31 (green) and α_{1B} (red), showing no colocalization. (C) ON from a rat with optic neuritis stained with SMI-32 (green), which labels nonphosphorylated axons, and α_{1B} (red) (arrows indicate points of colocalization). (D) Some glial fibrillary acidic protein–positive cells (green) were observed to express α_{1B} (red) (closed arrows indicate a colabeled cell). (E, F) Colocalization of the microglial/macrophage markers ED1 (E, green) and EMAP II (F, green) with α_{1B} (E, F red) during optic neuritis. Arrows indicate colabeled cells. (G, H) Colocalization between the oligodendrocytic marker CNPase (green) and α_{1B} (red) was not observed (H is a higher-power image of G). Scale bars = 20μm (A, D–F, H); 50μm (B, C); 100μm (G).

until day 21 after immunization, corresponding to a time point 1 week after disease manifestation. In the next two groups ("LATE"), delivery of ω-CTX or ve-

hicle started at EAE onset and was continued for 1 week.

In the PRE group, axon counts (given as the percentage of axon density compared with the average axon density in healthy ONs; n = 12) were improved when compared with vehicle-treated animals (ω-CTX
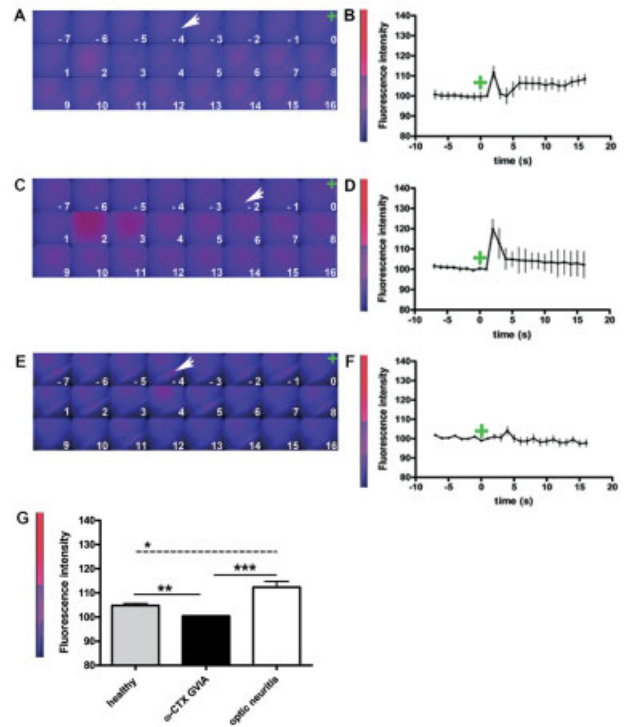
Fig 5. In vivo calcium imaging of rat optic nerves (ONs) after KCl-induced depolarization. (A, C, E) Microscopic view of a part of the ON, showing Ca-sensitive fluorescence intensity (FI) before and after KCl application. The time line in seconds is shown by numbers. Green crosses indicate time of KCl application (time 0) in the graphs and images. A thread (white arrowheads), placed around the ON, served as a spatial marker to ensure imaging of the same region during the whole duration of the measurements. (A) Healthy ON showing a mild FI increase after KCl application (segment 2). (B) FI in healthy ONs plotted against time. (C) Inflamed ON without application of ω-conotoxin GVIA (ω-CTX) showing an increase in FI after depolarization (segments 2–3). (D) FI in inflamed ONs without ω-CTX plotted against time. (E) Inflamed ON treated topically with ω-CTX showing mild FI increase after KCl application (segments 3–4). (F) FI in inflamed ONs with ω-CTX plotted against time. Note the reduction in FI after application of KCl when compared with (C, D). (G) Quantification of FI changes in ONs from healthy rats and from rats suffering from optic neuritis with and without application of ω-CTX. Application of the N-type voltage-dependent calcium channel (VDCC) blocker led to highly significant reduction of FI. Healthy rats and animals with optic neuritis not treated with ω-CTX received normal saline instead of blocker-containing solution. Error bars represent standard error of the means. *$p < 0.05$; **$p < 0.01$; ***$p < 0.001$.
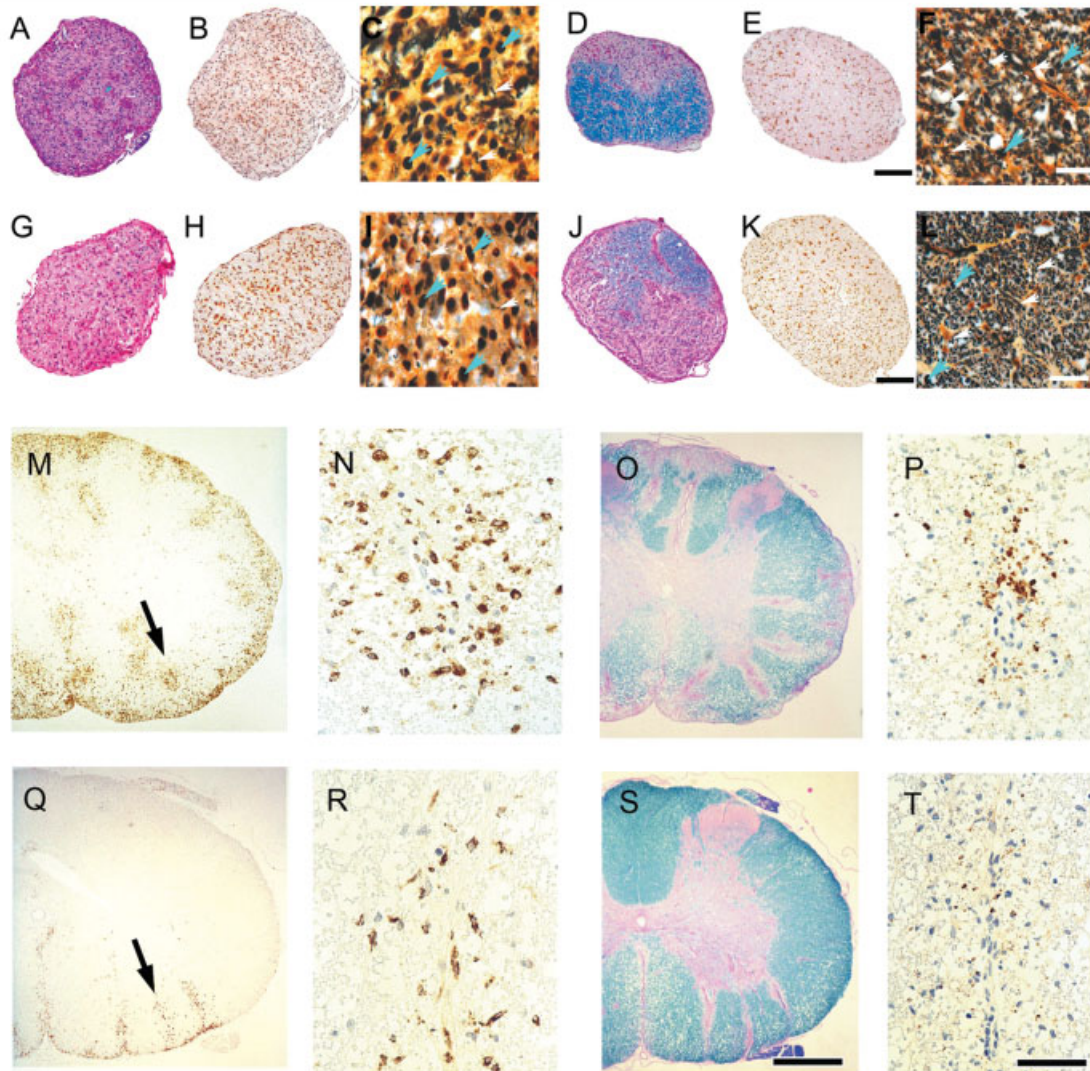
Fig 6. Effects of ω-conotoxin GVIA (ω-CTX) application on myelin oligodendrocyte glycoprotein (MOG)–induced optic neuritis and spinal cord lesions. Application of vehicle (A–C, G–I, M–P) or ω-CTX (D–F, J–L, Q–T) was either started two days before immunization (A–F, M–T) or given from the day of disease onset onward (G–L) and was continued over 3 weeks. (A, D, G, J) Luxol fast blue (LFB) staining of optic nerves (ONs) showing the extent of demyelination (purple areas). Blue areas indicate intact myelin. Note the decrease in demyelination in both ONs treated with ω-CTX (D, J). (C, F, I, L) Bielschowsky staining of ONs indicating the extent of axonal degeneration. White arrowheads *point to normal-appearing axons, whereas* green arrowheads *show infiltrating macrophages. Note the higher density of axons in both ω-CTX–treated ONs (F, L). (B, E, H, K) Immunohistochemistry for α_{1B} shows generally decreased expression in both ω-CTX–treated ONs (E, K) in comparison with the vehicle-treated ONs (B, H). (M, N, Q, R) Spinal cord sections obtained from a vehicle-treated rat (M, N) and a rat from the ω-CTX PRE-treated group (Q, R). Areas indicated by* black arrows *(M, Q) have been selected for higher magnification (N, R). Note that the vehicle-treated animal exhibited marked infiltration with ED1-positive cells perivascularly, in the meninges and in the parenchyma adjacent to the pia mater (M, N), whereas after ω-CTX treatment, infiltration with ED1-positive cells was sparse (Q, R). (O, S) LFB stainings of spinals cords showed confluent perivascular and subpial demyelination after vehicle treatment (O). In rats treated with ω-CTX, demyelination was restricted to small perivascular rims (S). (P, T) Spinal cord sections stained for β-amyloid precursor protein (β-APP). In animals treated with ω-CTX, β-APP–positive axons were only occasionally detectable (T). (P, T) Panels represent the same areas of the spinal cord as shown in (N, R). Scale bars = 100μm (A, B, D, E, G, H, J, K); 20μm (C, F, I, L); 300μm (M, O, Q, S); 50μm (N, P, R, T).*

treated, 9.6 ± 3.6%, n = 8; vehicle treated, 52.8 ± 8.2%, n = 5; $p < 0.01$; Figs 6C, 6F, and 7C). In the LATE group, a trend toward increased axon counts was seen after ω-CTX treatment; however, this differ-

ence was not statistically significant (ω-CTX treated, 13.9 ± 6.7%, n = 8; vehicle treated, 39.72 ± 6.3%, n = 5; $p = 0.06$; see Figs 6I, 6L, and 7D).

We further detected significantly reduced demyeli-
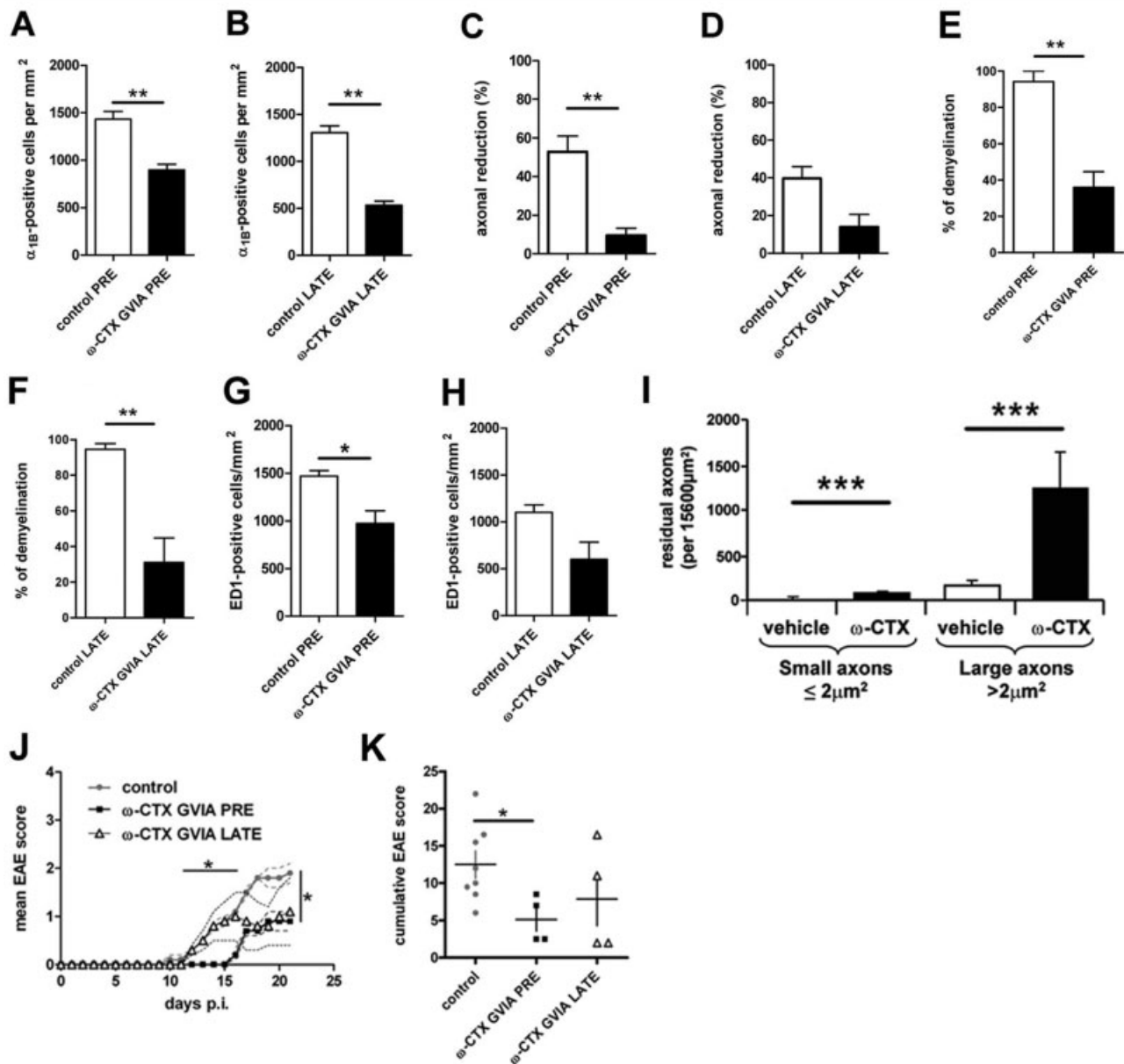
Fig 7. *Quantitative analyses of optic nerve (ON) histopathology and clinical course after PRE and LATE ω-conotoxin GVIA (ω-CTX) treatment in comparison with the vehicle-treated control groups. (A, B)* α_{1B} *expression is significantly reduced in the ω-CTX–treated groups, both in PRE (A) and LATE (B) treatment. (C, D) Percentage of axonal reduction is significantly reduced after PRE treatment (C), whereas in the LATE treatment group (D), there is a strong decreasing trend. (E, F) Percentage of demyelination is significantly reduced in the ω-CTX–treated groups, both after PRE (E) and LATE (F) treatment. (G, H) The number of ED1-positive cells is significantly reduced after ω-CTX PRE treatment (G). In the LATE group, there is a strong trend toward lower numbers of ED1-expressing cells after ω-CTX treatment (H). (I) Analysis of residual ON axons with different diameters after vehicle or ω-CTX treatment. Differentiation between axons with larger diameter ($>2\mu m^2$) and those with smaller diameter ($\leq 2\mu m^2$) demonstrated highly significant differences between the groups. (J, K) Mean clinical scores (J) and mean cumulative scores (K) were significantly lower in the group that received ω-CTX as a PRE treatment. The onset of experimental autoimmune encephalomyelitis (EAE) was significantly delayed in the ω-CTX PRE-treated group as well (J). For clearer presentation, the animals from the control groups are pooled together. Error bars in (A–I) and* dotted lines *in J represent standard error of the means.* *$p < 0.05$; **$p < 0.01$; ***$p < 0.005$. p.i. = postimmunization.

nation in both groups receiving ω-CTX compared with the vehicle-treated groups (ω-CTX PRE, 35.9 ± 8.7%, n = 8; vehicle PRE, 94.2 ± 5.8%, n = 5; *p* < 0.01; see Figs 6A, 6D, and 7E; ω-CTX LATE, 31.0 ± 13.7%, n = 8; vehicle LATE, 94.5 ± 3.2%, n = 5; *p* < 0.01; see Figs 6G, 6J, and 7F). In addi-

tion, we found significantly reduced numbers of infiltrating macrophages/microglia (given as ED1-positive cells/mm^2) in the ONs after PRE treatment (ω-CTX PRE, 975.3 ± 130.6, n = 8; vehicle PRE, 1,471 ± 58.7, n = 5; $p < 0.05$; see Fig 7G). In the LATE group treated with ω-CTX, there was a trend toward reduced inflammatory infiltration within the ONs (see Fig 7H). RGC counts did not differ between the ω-CTX– and vehicle-treated groups (data not shown).

Quantitative analysis of α_{1B} immunoreactivity demonstrated a significant reduction in the number of α_{1B}-positive sites per square millimeter in both the PRE and LATE ω-CTX–treated groups. In the PRE ω-CTX–treated group, the number of α_{1B}-positive sites per square millimeter was 899.7 ± 57.7 (n = 8), whereas for the vehicle-treated group, the value was 1,434 ± 80.4 (n = 5, $p < 0.01$; see Fig 7A). For the LATE treatment, the values in the ω-CTX–treated group were 532.8 ± 44.9 (n = 8), whereas the vehicle-treated controls had 1,306 ± 72.9 α_{1B}-positive sites per square millimeter (n = 5, $p < 0.01$) (mean ± standard error of the mean; see Fig 7B). ON sections from the different groups stained for α_{1B} are given in Figures 6B, E, H, and K. In parallel, spinal cord sections of healthy rats treated with ω-CTX or vehicle (n = 4 each) were stained for α_{1B}. The expression of α_{1B} in these groups did not differ (data not shown), indicating that binding of ω-CTX does not inhibit binding of the specific N-type VDCC antibody.

To examine a differential effect of ω-CTX on axon fibers of different diameters, we categorized remaining axons within demyelinated areas of the ONs as either large or small, using a size range of more than 2μm^2 for the large fibers and ≤2μm^2 for the small ones. Significantly more remaining axons of smaller diameter were observed in both ω-CTX–treated groups when compared with vehicle-treated animals ($p < 0.005$; see Fig 7I). Likewise, comparing remaining axons of larger diameter, we detected a significant difference between ω-CTX– and vehicle-treated animals ($p < 0.005$; see Fig 7I). However, the ratio of larger-diameter to smaller-diameter axons was 1:10.45 in the vehicle-treated animals (both groups were analyzed together) and 1:19.11 in the ω-CTX–treated animals, demonstrating a greater protective effect of ω-CTX on smaller-diameter axons.

Clinical Disease Course and Spinal Cord Lesions under ω-CTX Treatment
For the PRE treatment, disease onset was significantly delayed in the group that received ω-CTX (day 15.8 ± 0.9 after immunization; n = 4) in comparison with the control group (13.0 ± 0.7; n = 4; $p < 0.05$), and the cumulative score was significantly reduced (ω-CTX

Table. Summary of Histopathological Analyses of the Spinal Cord

Analysis	Mean ± SEM	p
Demyelination score		0.031
ω-CTX	0.50 ± 0.129	
Vehicle	1.25 ± 0.25	
ED1-positive cells/mm^2		0.046
ω-CTX	214.63 ± 100.96	
Vehicle	642.40 ± 157.60	
APP-positive axons/mm^2		0.025
ω-CTX	14.03 ± 10.07	
Vehicle	70.00 ± 22.65	

Summary of inflammation, demyelination, and acute axonal injury in the spinal cord in vehicle-treated compared with ω-conotoxin GVIA (ω-CTX)–treated animals (the PRE and LATE groups were analyzed together). Quantitative analyses of the number of ED1-positive cells (activated macrophages/microglia), expressed as ED1-positive cells per square millimeter per total cross section of the spinal cord, and the number of β-amyloid precursor protein (β-APP)–positive axons expressed as β-APP–positive axons per square millimeter per total cross section of the spinal cord in the vehicle-treated and ω-CTX–treated groups. Demyelination was evaluated semiquantitatively as described in Materials and Methods. ω-CTX–treated animals showed significantly lower degrees of demyelination. The number of ED1-positive cells and the number of injured axons were significantly reduced in ω-CTX–treated animals compared with vehicle treatment. SEM = standard error of the mean.

treated, 5.1 ± 1.5; vehicle treated, 12.5 ± 1.8; $p < 0.05$). In the LATE groups (n = 4 each), neurological outcome was not significantly improved after ω-CTX treatment (cumulative score, 7.9 ± 3.6) compared with vehicle treatment, although two of the four rats did improve. The disease course and the cumulative scores of the different animal groups are given in Figures 7J and K.

In general, spinal cord pathology in most of the rats was characterized by perivascular inflammation and demyelination. Inflammatory infiltrates were present around veins and venules, and inflammation was also localized in the meninges with dispersion to the parenchyma adjacent to the pia mater. Inflammation mainly consisted of ED1-positive macrophages and few W3/13-positive T cells.

In accordance with the clinical data, quantitative histopathological examination of the spinal cords demonstrated significantly lower numbers of ED1-positive cells in ω-CTX–treated animals around veins and/or in the parenchyma adjacent to the pia mater ($p < 0.05$; Table; see Figs 6Q, R) when compared with vehicle-treated rats (ω-CTX–treated and vehicle-treated groups were analyzed together). Reduced inflammation was associated with significantly lower demyelination scores compared with the vehicle-treated

group and restricted to small rims of perivascular demyelination ($p < 0.05$; see the Table, see Fig 6S). Axons immunoreactive for β-APP were present to a significantly lower degree in ω-CTX–treated animals compared with the vehicle-treated group ($p < 0.05$; see the Table, see Fig 6T). In contrast, the vehicle-treated group exhibited pronounced perivascular inflammation and abundant inflammation in the parenchyma adjacent to the pia mater (see the Table; see Figs 6M, N) associated with confluent subpial and perivenous demyelination (see the Table; see Fig 6O), and prominent acute axonal injury demonstrated by immunoreactivity for β-APP (see the Table; see Fig 6P).

Discussion

In a broader disease context than MS, neuroprotective effects of N-type VDCC antagonists have been described using models of ischemia, brain trauma, and neuropathic pain.[33,36,37] However, to date, no studies have investigated the effects of N-type VDCC antagonists on neurodegeneration and inflammation under autoimmune conditions. Continuous application of ω-CTX in our study led to axon protection when started before immunization. Although a trend toward a decreased number of degenerating axons was observed on administration of ω-CTX from disease onset, this did not prove to be significant. This is in agreement with our earlier studies, in which application of erythropoietin rescued neurons only if the treatment was given prophylactically[11,38] and is explained by characteristics of our model, in which neurodegeneration starts before the onset of clinical symptoms.[8] At the time of disease manifestation, axonal damage within the ON had progressed[6] such that therapeutic interventions targeting early pathophysiological events are too late.

The application of ω-CTX in our study not only protected axons that upregulate N-type VDCCs but also reduced demyelination and inflammatory infiltration within the ON. To investigate whether the effect on demyelination is a primary phenomenon resulting from a blockade of N-type VDCCs expressed on oligodendrocytes, we performed costainings of N-type VDCCs and CNPase. Because no oligodendroglial expression of the channels could be detected, this effect might either be secondary to axonal protection or result from the decreased amount of inflammatory infiltration. Because we showed that N-type VDCCs are expressed on macrophages/microglia, it is possible that the decreased demyelination is caused by reduced activation of macrophages/microglia under treatment with ω-CTX. In support of this notion, there is evidence that VDCCs are involved in microglial activation and superoxide anion production.[39] There is a notable parallel between our results on N-type VDCCs and pre-vious data on other voltage-gated cation channels. Craner and colleagues[40] and Carrithers and coauthors[41] showed that sodium channels influence macrophage and microglia activity in neuroinflammatory disorders. Furthermore, it was demonstrated that sodium channel subtypes such as $Na_v1.6$ are colocalized with the Na^+/Ca^{2+} exchanger in degenerating axons in mice with EAE, as well as in acute lesions in patients with MS.[42,43] Similar to the dual role for N-type VDCCs proposed in our study, Waxman[44] noted that sodium channels appear to play two parallel roles in neuroinflammatory disease: First, they permit ion fluxes that directly injure axons, and second, they exert immunomodulatory effects. Another similarity between N-type VDCCs and voltage-gated sodium channels is their expression on astrocytes. Sontheimer and coauthors[45,46] reported that voltage-gated sodium channels are present[45] and functional[46] on astrocytes. Whereas, among other functions, sodium channels appear to be important for maintaining the activity of the Na^+/K^+-ATPase in these nonexcitable cells,[46] VDCCs in astrocytes may be involved in the release of neurotrophic factors, ionic homeostasis, and glial network signaling.[47,48]

It is possible that the Mn^{2+} enhancement we detected within inflamed ONs results from an uptake of this ion via axonal N-type VDCCs that are upregulated in degenerating ON axons. However, it is also possible that the contrast agent is taken up by macrophages/microglia or astrocytes as our double-labeling studies showed N-type VDCC expression on both ED1-/EMAP II– and GFAP-positive cells. This hypothesis is supported by studies showing Mn^{2+} uptake by astrocytes and microglia, and a correlation between hyperintense areas in Mn^{2+}-enhanced MRI and areas of microglial activation.[49,50]

In our study, we found no effect of ω-CTX on RGC survival. This might be explained by a differential expression of VDCCs in the somata and axons of RGCs. Previous studies investigating somatic expression of VDCCs in dorsal root ganglion neurons after sciatic nerve injury showed a reduced expression of the N-type.[51] Alternatively, the selective axonal protection by ω-CTX could be caused by an independent pathophysiology of neuronal and axonal damage in our model. This hypothesis is supported by earlier observations showing that a proportion of RGCs die because of electrophysiological dysfunction during the induction phase of optic neuritis, independent of morphologically detectable axonal damage.[8]

For the mechanisms that underlie the potential N-type VDCC upregulation observed in demyelinated axons, we propose a scenario that is supported by studies on metabolism and trafficking of N-type VDCCs.[52,53] In these studies, a large intraneuronal pool of recruitable N-type VDCCs was observed. In our model

of optic neuritis, we detected a colocalization of α_{1B} and β-APP. This suggests that disturbances in axonal transport could lead to an accumulation of vesicles containing N-type VDCCs within demyelinating axons and their insertion to the membrane. This mechanism could possibly explain the greater protective effect of ω-CTX that we observed on smaller-diameter, as opposed to larger-diameter, axon fibers. Conceivably, insertion of N-type VDCCs into axonal membranes would result in a larger number of VDCCs per axonal volume in smaller axon fibers, permitting a greater pathological influx of Ca^{2+} into these smaller axons. This mechanism could also be an explanation for the preferential loss of small-diameter axons observed in MS.[21] Until this point, the scenario is similar to the one that Kornek and colleagues[4] proposed. However, considering observations made by Cavalie and colleagues,[54] who detected enhanced calcium currents in PC12 cells after cotransfection with c-*fos* and c-*jun,* an additional mechanism could be taken into account: The expression of high-voltage–activated VDCCs may be induced by immediate early genes at a transcriptional level. Therefore, we postulate that in parallel with the insertion of accumulated vesicles containing N-type VDCCs into the axonal membrane, immediate early genes induce synthesis of N-type VDCCs in neurons under autoimmune inflammatory conditions. Similarly, Craner and coauthors[55] showed increased sodium channel synthesis in RGC bodies during EAE. However, the question remains whether there is a global upregulation of transcription in autoimmune inflammation, or whether transcription is selectively upregulated for specific proteins. Craner and coauthors[55] reported not only increased synthesis of $Na_v1.2$ but also reduced expression of $Na_v1.6$ channels. Therefore, it is more likely that the phenomenon they observed is a switch in gene expression rather than a general upregulation. However, nuclear factor-κB, a transcription factor of global importance, has recently been linked to the pathophysiology of autoimmune demyelinating central nervous system diseases,[56] suggesting a way in which an upregulation of transcription might have more general effects.

Further studies are needed to explore the pathophysiological role of other VDCC types or AMPA/kainate receptors, or both, which have been shown to influence EAE,[26,57] and for which we observed some effect in Mn^{2+}-enhanced MRI.

References

1. Trapp BD, Ransohoff R, Rudick R. Axonal pathology in multiple sclerosis: relationship to neurologic disability. Curr Opin Neurol 1999;12:295–302.
2. Bitsch A, Schuchardt J, Bunkowski S, et al. Acute axonal injury in multiple sclerosis. Correlation with demyelination and inflammation. Brain 2000;123:1174–1183.
3. Losseff NA, Miller DH. Measures of brain and spinal cord atrophy in multiple sclerosis. J Neurol Neurosurg Psychiatry 1998;64:S102–S105.
4. Kornek B, Storch MK, Bauer J, et al. Distribution of a calcium channel subunit in dystrophic axons in multiple sclerosis and experimental autoimmune encephalomyelitis. Brain 2001;124:1114–1124.
5. Peterson JW, Bo L, Mork S, et al. Transected neurites, apoptotic neurons, and reduced inflammation in cortical multiple sclerosis lesions. Ann Neurol 2001;50:389–400.
6. Meyer R, Weissert R, Diem R, et al. Acute neuronal apoptosis in a rat model of multiple sclerosis. J Neurosci 2001;21:6214–6220.
7. Diem R, Hobom M, Maier K, et al. Methylprednisolone increases neuronal apoptosis during autoimmune CNS inflammation by inhibition of an endogenous neuroprotective pathway. J Neurosci 2003;23:6993–7000.
8. Hobom M, Storch MK, Weissert R, et al. Mechanisms and time course of neuronal degeneration in experimental autoimmune encephalomyelitis. Brain Pathol 2004;14:148–157.
9. Hauser SL, Oksenberg JR. The neurobiology of multiple sclerosis: genes, inflammation, and neurodegeneration. Neuron 2006;52:61–76.
10. Wekerle H, Kojima K, Lannes-Vieira J, et al. Animal models. Ann Neurol 1994;36:S47–S53.
11. Diem R, Sättler MB, Merkler D, et al. Combined therapy with methylprednisolone and erythropoietin in a model of multiple sclerosis. Brain 2005;128:375–385.
12. George EB, Glass JD, Griffin JW. Axotomy-induced axonal degeneration is mediated by calcium influx through ion-specific channels. J Neurosci 1995;15:6445–6452.
13. Fern R, Ransom BR, Waxman SG. Voltage-gated calcium channels in CNS white matter: role in anoxic injury. J Neurophysiol 1995;74:369–377.
14. Brown AM, Westenbroek RE, Catterall WA, et al. Axonal L-type Ca2+ channels and anoxic injury in rat CNS white matter. J Neurophysiol 2001;85:900–911.
15. Imaizumi T, Kocsis JD, Waxman SG. The role of voltage-gated Ca2+ channels in anoxic injury of spinal cord white matter. Brain Res 1999;817:84–92.
16. Stys PK. General mechanisms of axonal damage and its prevention. J Neurol Sci 2005;233:3–13.
17. Eder C. Ion channels in microglia (brain macrophages). Am J Physiol 1998;275:C327–C342.
18. Boucsein C, Kettenmann H, Nolte C. Electrophysiological properties of microglial cells in normal and pathologic rat brain slices. Eur J Neurosci 2000;12:2049–2058.
19. Badou A, Jha MK, Matza D, et al. Critical role for the beta regulatory subunits of Cav channels in T lymphocyte function. Proc Natl Acad Sci USA 2006;103:15529–15534.
20. Weissert R, Wallstrom E, Storch MK, et al. MHC haplotype-dependent regulation of MOG-induced EAE in rats. J Clin Invest 1998;102:1265–1273.
21. DeLuca GC, Ebers GC, Esiri MM. Axonal loss in multiple sclerosis: a pathological survey of the corticospinal and sensory tracts. Brain 2004;127:1009–1018.

22. Storch MK, Stefferl A, Brehm U, et al. Autoimmunity to myelin oligodendrocyte glycoprotein in rats mimics the spectrum of multiple sclerosis pathology. Brain Pathol 1998;8:681–694.

23. Kornek B, Storch MK, Weissert R, et al. Multiple sclerosis and chronic autoimmune encephalomyelitis: a comparative quantitative study of axonal injury in active, inactive, and remyelinated lesions. Am J Pathol 2000;157:267–276.

24. Storch MK, Weissert R, Birnbacher R, et al. MHC gene related effects on microglia and macrophages in experimental autoimmune encephalomyelitis determine the extent of axonal injury. Brain Pathol 2002;12:287–299.

25. Boretius S, Gadjanski I, Demmer I, et al. MRI of optic neuritis in a rat model. Neuroimage 2008;41:323–334.

26. Smith T, Groom A, Zhu B, et al. Autoimmune encephalomyelitis ameliorated by AMPA antagonists. Nat Med 2000;6:62–66.

27. Turner RJ, Van den Heuvel C, Vink R. Amiloride increases neuronal damage after traumatic brain injury in rats. J Am Coll Nutr 2004;23:534–537.

28. Akerman S, Williamson DJ, Goadsby PJ. Voltage-dependent calcium channels are involved in neurogenic dural vasodilatation via a presynaptic transmitter release mechanism. Br J Pharmacol 2003;140:558–566.

29. Sun BB, Chiu SY. N-type calcium channels and their regulation by GABAB receptors in axons of neonatal rat optic nerve. J Neurosci 1999;19:5185–5194.

30. Furukawa T, Nukada T, Suzuki K, et al. Voltage and pH dependent block of cloned N-type Ca2+ channels by amlodipine. Br J Pharmacol 1997;121:1136–1140.

31. Xiao WH, Bennett GJ. Synthetic omega-conopeptides applied to the site of nerve injury suppress neuropathic pains in rats. J Pharmacol Exp Ther 1995;274:666–672.

32. Malmberg AB, Yaksh TL. Effect of continuous intrathecal infusion of omega-conopeptides, N-type calcium-channel blockers, on behavior and antinociception in the formalin and hotplate tests in rats. Pain 1995;60:83–90.

33. Bowersox S, Mandema J, Tarczy-Hornoch K, et al. Pharmacokinetics of SNX-111, a selective N-type calcium channel blocker, in rats and cynomolgus monkeys. Drug Metab Dispos 1997;25:379–383.

34. Murray JC, Barnett G, Tas M, et al. Immunohistochemical analysis of endothelial-monocyte-activating polypeptide-II expression in vivo. Am J Pathol 2000;157:2045–2057.

35. Mueller CA, Schluesener HJ, Conrad S, et al. Lesional expression of a proinflammatory and antiangiogenic cytokine EMAP II confined to endothelium and microglia/macrophages during secondary damage following experimental traumatic brain injury. J Neuroimmunol 2003;135:3–9.

36. Valentino K, Newcomb R, Gadbois T, et al. A selective N-type calcium channel antagonist protects against neuronal loss after global cerebral ischemia. Proc Natl Acad Sci USA 1993;90:7894–7897.

37. Burns LH, Jin Z, Bowersox SS. The neuroprotective effects of intrathecal administration of the selective N-type calcium channel blocker ziconotide in a rat model of spinal ischemia. J Vasc Surg 1999;30:334–343.

38. Sättler MB, Merkler D, Maier K, et al. Neuroprotective effects and intracellular signaling pathways of erythropoietin in a rat model of multiple sclerosis. Cell Death Differ 2004;11(suppl 2):S181–S192.

39. Colton CA, Jia M, Li MX, et al. K+ modulation of microglial superoxide production: involvement of voltage-gated Ca2+ channels. Am J Physiol 1994;266:C1650–C1655.

40. Craner MJ, Damarjian TG, Liu S, et al. Sodium channels contribute to microglia/macrophage activation and function in EAE and MS. Glia 2005;49:220–229.

41. Carrithers MD, Sulayman DH, Carrithers LM, et al. Expression of the voltage-gated sodium channel $Na_V1.5$ in the macrophage late endosome regulates endosomal acidification. J Immunol 2007;178:7822–7832.

42. Craner MJ, Hains BC, Lo AC, et al. Co-localization of sodium channel $Na_v1.6$ and the sodium-calcium exchanger at sites of axonal injury in the spinal cord in EAE. Brain 2004;127:294–303.

43. Craner MJ, Newcombe J, Black JA, et al. Molecular changes in neurons in multiple sclerosis: altered axonal expression of $Na_v1.2$ and $Na_v1.6$ sodium channels and Na+/Ca2+ exchanger. Proc Natl Acad Sci USA 2004;101:8168–8173.

44. Waxman S. Mechanisms of disease: sodium channels and neuroprotection in multiple sclerosis-current status. Nat Clin Pract Neurol 2008;4:159–169.

45. Sontheimer H, Waxman SG. Ion channels in spinal cord astrocytes in vitro. II. Biophysical and pharmacological analysis of two Na+ current types. Neurophysiology 1992;68:1001–1111.

46. Sontheimer H, Fernandez-Marques E, Ullrich N, et al. Astrocyte Na+ channels are required for maintenance of Na^+/K^+-ATPase activity. J Neurosci 1994;14:2464–2475.

47. Westenbroeck RE, Bausch SB, Lin RCS, et al. Upregulation of L-type Ca^{2+} channels in reactive astrocytes after brain injury, hypomyelination and ischemia. J Neurosci 1998;18:2321–2334.

48. D'Ascenzo M, Vairano M, Andreassi C, et al. Electrophysiological and molecular evidence of L-(Ca_v1), N-($Ca_v2.2$), and R-($Ca_v2.3$) type Ca^{2+} channels in rat cortical astrocytes. Glia 2004;45:354–363.

49. Alvestad S, Goa PE, Qu H, et al. In vivo mapping of temporospatial changes in manganese enhancement in rat brain during epileptogenesis. NeuroImage 2007;38:57–66.

50. Haapanen A, Ramadan UA, Autti T, et al. In vivo MRI reveals the dynamics of pathological changes in the brains of cathepsin D-deficient mice and correlates changes in manganese-enhanced MRI with microglial activation. Magn Reson Imaging 2007;25:1024–1031.

51. Baccei ML, Kocsis JD. Voltage-gated calcium currents in axotomized adult rat cutaneous afferent neurons. J Neurophysiol 2000;83:2227–2238.

52. Sher E, Rosa P, Francolini M, et al. Metabolism and trafficking of N-type-operated calcium channels in neurosecretory cells. J Bioenerg Biomembr 1998;30:399–407.

53. Passafaro M, Rosa P, Sala C, et al. N-type Ca2+ channels are present in secretory granules and are transiently translocated to the plasma membrane during regulated exocytosis. J Biol Chem 1996;271:30096–30104.

54. Cavalie A, Berninger, Haas CA, et al. Constitutive upregulation of calcium channel currents in rat phaeochromocytoma cells: role of c-fos and c-jun. J Physiol 1994;479(pt 1):11–27.

55. Craner MJ, Albert CL, Black JA, Waxman SG. Abnormal sodium channel distribution in optic nerve axons in a model of inflammatory demyelination. Brain 2003;126:1552–1561.

56. van Loo G, De Lorenzi R, Schmidt H, et al. Inhibition of transcription factor NF-kappaB in the central nervous system ameliorates autoimmune encephalomyelitis in mice. Nat Immunol 2006;7:954–961.

57. Brand-Schieber E, Werner P. Calcium channel blockers ameliorate disease in a mouse model of multiple sclerosis. Exp Neurol 2004;189:5–9.